agriculture

MDPI

Article

Optimization of Rotary Blade Wear and Tillage Resistance Based on DEM-MBD Coupling Model

Zhiqiang Mao [1], Yang Zhang [1,*], Keping Zhang [1], Jiuxin Wang [1], Junqian Yang [1], Xiaobao Zheng [1], Shuaikang Chen [1], Zhongqing Yang [1] and Biao Luo [2]

[1] College of Mechanical and Electrical Engineering, Gansu Agricultural University, Lanzhou 730070, China; 1073323120396@st.gsau.edu.cn (Z.M.); zhangkp@gsau.edu.cn (K.Z.); wjx@gsau.edu.cn (J.W.); yangjq93@163.com (J.Y.); zhengxb0915@163.com (X.Z.); chenshuaikang6@163.com (S.C.); 17793047953@163.com (Z.Y.)

[2] College of Civil Engineering, Hunan University, Changsha 410082, China

* Correspondence: zhangyang@gsau.edu.cn

Abstract: To solve the problems of high tillage resistance and the rapid wear of the rotary blade during tillage, this study employed a coupled algorithm of the discrete element method (DEM) and multi-body dynamics (MBD) with Hertz–Mindlin with JKR particle contact theory to establish a rotary blade–sandy soil model. The interaction between the rotary blade and sandy soil was analyzed. The results indicated that the lateral and horizontal resistances of the rotary blade reached the peak values near the maximum tilling depth, whereas the vertical resistance reached its peak earlier. Blade wear predominantly occurred on the side cutting edge, bending zone edge, and sidelong edge, with the most significant wear observed on the sidelong edge, followed by the bending zone edge and side cutting edge, which showed similar wear patterns. To reduce wear and tillage resistance, Box–Behnken optimization was applied to optimize the blade's local parameters. The optimal parameters—the height of the tangent edge end face was 51 mm, the bending radius was 28 mm, and the bending angle was 116°—reduced wear by 22.4% and tillage resistance by 12%. A soil disturbance analysis demonstrated that the optimized blade performs better in terms of tillage width compared to the unoptimized blade. The optimized rotary blade achieves the effects of reduced resistance and wear, improves the lifespan of the blade, reducing material loss, and meeting the requirements of sustainable agricultural production.

Keywords: rotary blade; sandy soil environment; DEM-MBD coupling; reduce resistance and wear; local optimization; soil disturbance

Academic Editor: Takashi Okayasu

Received: 3 January 2025
Revised: 26 January 2025
Accepted: 31 January 2025
Published: 2 February 2025

Citation: Mao, Z.; Zhang, Y.; Zhang, K.; Wang, J.; Yang, J.; Zheng, X.; Chen, S.; Yang, Z.; Luo, B. Optimization of Rotary Blade Wear and Tillage Resistance Based on DEM-MBD Coupling Model. *Agriculture* **2025**, *15*, 328. https://doi.org/10.3390/agriculture15030328

1. Introduction

The rotary blade, as a key component of the rotary tiller, primarily performs periodic tasks such as cutting, breaking, and throwing soil. However, the blade is in constant direct contact with impurities such as stones, gravel, and crop residues in sandy and stony soils; this not only subjects the blade to impacts from various directions, increasing the tillage resistance during the soil cultivation process, but also accelerates wear on the blade, reducing the machine's operational efficiency and the quality of soil tillage [1]. This results in the failure to meet agronomic standards, significantly raises replacement costs [2], delays farming schedules, and hinders the development of intelligent agricultural machinery. Reducing tillage resistance and enhancing the wear resistance of soil-engaging

components have become key strategies for promoting the high-quality development of agricultural equipment.

At present, existing research has proposed methods, such as structural design, biomimicry, and simulation modeling, to improve the wear resistance of rotary blades. For example, Zhang et al. [3] used CCF (central composite face-centered design) to carry out the simulation of soil cutting and analyzed the effects of various factors on three-axis working resistances by the RSM (surface response method), and optimized the rotary blade structure by Design-Expert. Zhu et al. [4] designed a reverse rotary tilling excavation device, and conducted a comparison between simulations and field experiments, finding that the simulation analysis of the rotary blade has a high feasibility in the study of resistance reduction and wear reduction. Li et al. [5] used the SPH model for soil cutting simulations to reduce the power consumption of rotary tillage operations and optimized the rotary blade based on various influencing factors. Sun et al. [6] designed three new types of blades and established a blade–soil interaction model based on the SPH model to compare and analyze the soil disturbance of the new blades and existing blades. Wang et al. [7] found that the current research mainly investigates soil disturbance trends through tracers. Zhang et al. [8] established a soil disturbance model to test four different plows, analyzing the soil disturbance effects of these plows and quantifying the loosening effect of compacted grassland based on the Soil Disturbance Index (SDI).Yang et al. and Zhang et al. [9,10] designed different biomimetic structures based on the characteristics of various organisms. The experiment showed that the bionic structure exhibited a better resistance reduction and wear reduction effect.

Moreover, due to the significant differences in soil composition across different regions, biomimetic technology and structural design face limitations in practical applications. These methods can only adapt to specific soil conditions, making it difficult to achieve their widespread application in complex and variable soil types. In recent years, the discrete element method (DEM) has become an important research tool [11–14], which can directly simulate the interaction mechanism between the soil-engaging component and soil to optimize the parameters of the tool [15]; however, DEM-MBD coupling simulation can better reflect the dynamic analysis of the rotary blade than the DEM simulation alone. At the same time, 3D scanning has also been introduced into soil-engagement research for reverse modeling to improve the simulation accuracy. For example, Chen et al. and Song et al. [16,17] optimized the parameters of soil-engaging components by DEM-MBD simulation to significantly reduce its tillage resistance. Yuan et al., Liu et al., Zhang et al., and Dong et al. [18–21] analyzed the resistance reduction mechanisms and interaction mechanisms between soil-engaging components and soil based on the DEM-MBD coupling algorithm. Tekeste M. Z. et al. and Cucinotta F. et al. [22–24] used 3D scanning technology to reconstruct the solid models of various soil-engaging components, and combined it with discrete element simulation to explore the interaction mechanisms and wear mechanisms between soil-engaging components and soil in depth. In order to explore the variation law of the three-dimensional resistance of rotary blades, Xiong et al. [25] reconstructed the rotary blade entity in reverse by 3D scanning and established the rotary blade–soil interaction simulation model.

In summary, the current research focuses on the biomimetic and structural design of soil-engaging components, but these two methods have certain limitations in specific regions. Moreover, previous studies usually optimize the rotary blade based on a single evaluation index, and few people optimize the local parameters for the wear and tillage resistance of the soil-engaging components at the same time. Considering the two evaluation indexes of tillage resistance and wear can analyze and optimize the rotary blade from the perspectives of macroscopic force and the microscopic wear mechanism and improve the

comprehensive performance of the rotary blade. Therefore, this study takes the wear and resistance characteristics of rotary blades as the starting point and combines DEM-MBD coupling simulation to construct a rotary blade–soil interaction model; the aim is to explore the working mechanism of the rotary blade in a sandy and gravelly soil environment, revealing areas of the blade that are prone to wear and high resistance. Based on this, the study proposes optimizing the local parameters of the rotary blade, aiming to reduce resistance and wear, thereby extending its service life.

2. Materials and Methods

2.1. The Structure and Working Principle of the Blade Roller

As shown in Figure 1a, the blade roller is a combined operating component suspended at the rear of the tractor. This mechanism mainly consists of the rotary blade shaft, rotary blades, gearbox, frame, lifting lever, and retaining plate and is connected to the tractor with the three-point suspension device. The drive system includes a gearbox that drives the rotation of the rotary blade shaft and a hydraulic system that lifts the blade roller. The main power for the blade roller comes from the tractor's output shaft, which transmits power to the input shaft of the gearbox. After the gearbox adjusts the speed and direction of transmission, the power is transmitted through the output shaft to the rotary blade shaft, driving the rotation of the rotary blades. At the same time, the machine moves forward in a constant-speed straight line. The hydraulic system lowers the frame and blade roller to the appropriate working depth, where the rotary blades are in contact with the soil for cutting, turning, and crushing. It cuts the compacted soil into small clods, which are then thrown backward by the rotating blade roller, forming a relatively flat surface under the obstruction of the baffles.

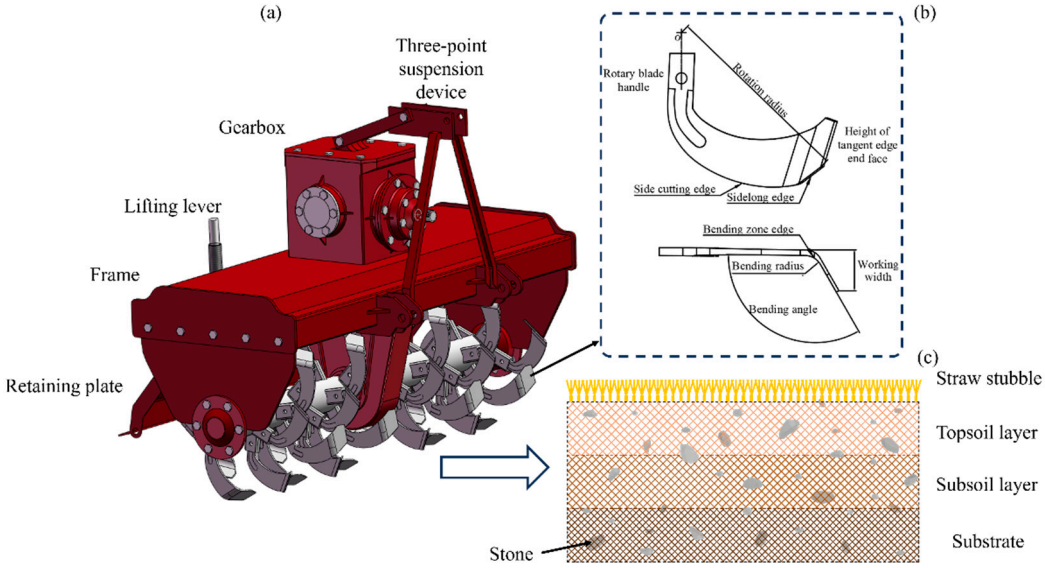

Figure 1. Structure of blade roller and rotary blade. (**a**) Structure of blade roller; (**b**) structure of rotary blade; and (**c**) tillage environments for rotary blades.

As shown in Figure 1c, the soil is divided into three layers, from top to bottom as follows: the topsoil layer, the subsoil layer, and the substrate layer. The main working area of the rotary blades is the topsoil layer and the soil surface, which contain many adverse factors such as stones, gravel, and crop residues. These factors accelerate the wear of the rotary blades and severely affect the working efficiency of the rotary tiller.

2.2. Model and Arrangement of the Rotary Blade

The rotary blade, made of 65 Mn steel, is selected as the research object (the height of its tangent edge end face is 56 mm, the bending radius is 25 mm, the bending angle is 120°, and the rotation radius is 245 mm). It is difficult to use traditional modeling methods to accurately draw the curves of the rotary blade, and there will be a large error. Therefore, a 3D laser scanner (model: FARO Laser ScanArm, scanning accuracy: 16 microns) is used to scan the surface of the rotary blade to obtain the point cloud data, and then the point cloud data are repaired using Geomagic Studio. Subsequently, based on the shape of the point cloud model, reverse modeling is performed using Design X. The model is exported in .stp format and imported into SolidWorks. The final rotary blade model is shown in Figure 1b. The correlation coefficient between the reverse modeling and scanned rotary blade is calculated to be R = 0.98, which indicates that the accuracy of the reverse modeling is high.

To ensure the efficiency and uniformity of soil crushing, and to facilitate the soil offset to the center, the layout of the rotary blades is shown in Figure 2. The overall design adopts a symmetrical herringbone arrangement. The installation direction of the rotary blades is adjusted so that the blades rotate to the centerline. The single-sided blade roller uses an alternating arrangement of left and right blades. The angle between the left and right blades on the same rotational plane is set to 180°, and the angle between adjacent blades along the same helical axis is set to 72°. The spacing between adjacent rotational planes is 33 mm.

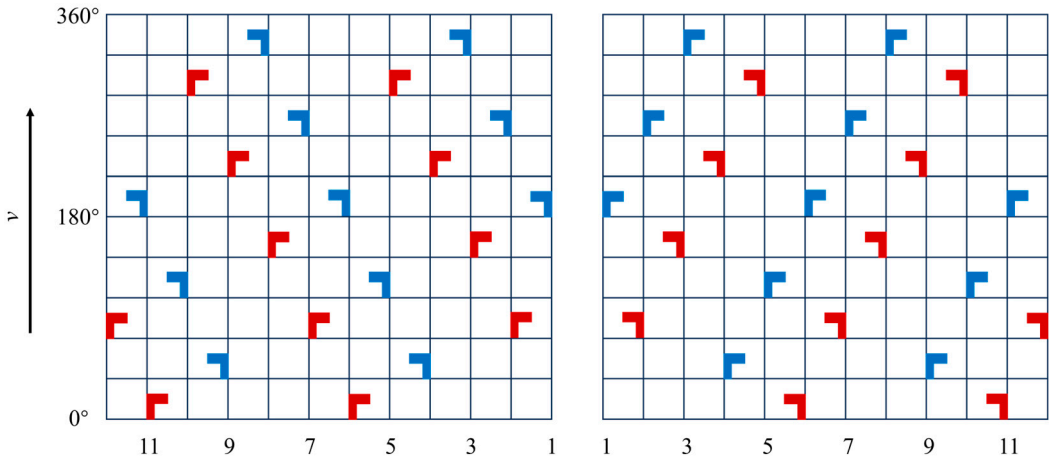

Figure 2. Schematic diagram of planar arrangement of rotary blades. Red indicates that the tip of the rotary blade bends toward the center, and blue represents that the tip of the rotary blade bends toward the outside.

2.3. Analysis of Dynamics and Wear Mechanism of the Rotary Blade

2.3.1. Motion Trajectory of the Rotary Blade

The motion trajectory of the rotary blade in the process of plowing is shown in Figure 3 as a cosine line [26], which is mainly a composite motion of the blade's forward speed and the rotational speed around the blade shaft. Establish the *XOY* plane coordinate system, set the forward direction of the blade shaft as the positive direction of the *X*-axis, and set the vertical soil plane upwards as the positive direction of the *Y*-axis. The moving trajectory of the rotary blade can be expressed as follows:

$$\begin{cases} x = V_m t + R\cos\theta \\ y = -R\sin\theta \end{cases} \quad (1)$$

where V_m is the forward speed of the rotary blade (m·s^{-1}); R is the rotational radius of the rotary blade (mm); ω is the angular velocity of the rotary blade (rad·s^{-1}); and θ is the tillage angle of the rotary blade (°).

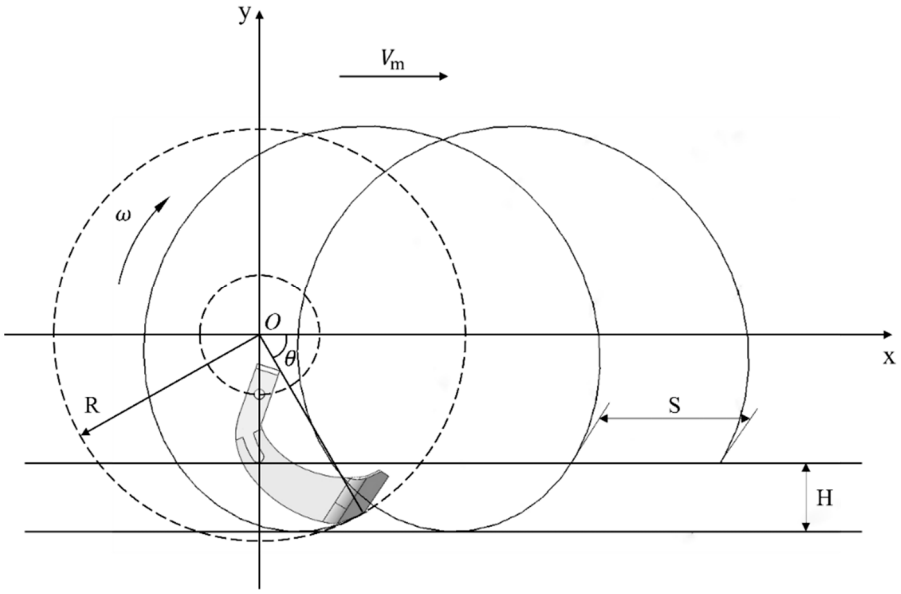

Figure 3. Moving trajectory of the rotary blade. H is the tillage depth of the rotary blade (mm); and θ is the tillage angle of the rotary blade (°).

In order to ensure that the rotary blade can work properly, the ratio of the tip circumferential speed to the forward speed of the rotary blade (i.e., the rotary tillage speed ratio λ) needs to be greater than 1. When $\lambda < 1$, the direction of the horizontal partial velocity of the rotary blade tip is always towards the front, resulting in the rotary blade not being able to throw the soil backward and appearing to push the soil forward, so the larger the rotary tillage speed ratio λ, the better the effect of cutting the soil, and the rotary tillage speed ratio λ is as follows:

$$\lambda = \frac{2\pi R}{SZ} \tag{2}$$

where S is the cutting spacing of the soil (mm); Z is the number of blades in a single turn of the blade shaft; and R is the rotational radius of the rotary blade (mm).

The cutting spacing S represents the distance between two consecutive cuts of the soil by the rotary blade [27]. Cutting spacing has a direct effect on the quality of the crushed soil and the tillage resistance, with too much spacing leading to an increase in the thickness of the soil cutting and reducing tillage quality.

According to the above formula, when the rotary radius of the rotary blade R is 245 mm, the number of blades in a single circle Z is 3, and the cutting spacing S is usually taken as 90~150 mm, which can be brought into Equation (2) to obtain the rotary tillage speed ratio λ as 3.42~5.7, which satisfies the normal working conditions. The forward speed of the tool V_m can also be obtained from the rotary tillage speed ratio as follows:

$$V_m = \frac{n}{60\lambda} \tag{3}$$

where n is the rotational speed of the blade shaft (r·min^{-1}); and λ is the rotary tillage speed ratio.

Set the rotational speed of the blade shaft n to 150 r/min, and the forward speed of the rotary blade V_m can be calculated as 0.44–0.73 m/s, and finally, approximate the selection as 0.5 m/s.

2.3.2. Force Analysis of the Rotary Blade

In the process of tilling, the side cutting edge and sidelong edge of the rotary blade cut into the soil successively, completing the cyclic movement of cutting, breaking, and throwing [28]. Any cutting section of the left rotary blade can be selected as the object to analyze its force characteristics. When the blade edge contacts the soil, it experiences an upward force F_p from the soil. After the rotary blade cuts into the soil, the surface generates sliding friction f_i and inward pressure F_i from the soil, and Figure 4 is the force analysis diagram of the cutting cross-section of the rotary blade.

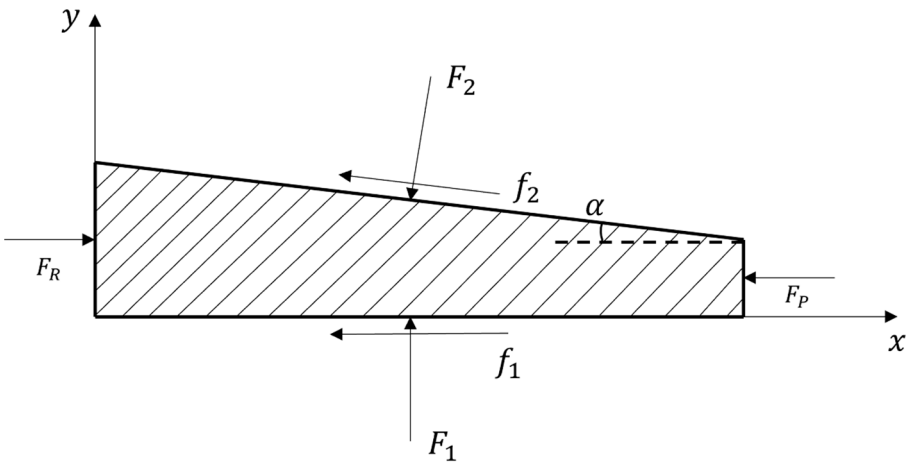

Figure 4. Cross-sectional force diagram of rotary blade.

The formulas for the vertical and horizontal forces on the rotary blade and the sliding friction between the rotary blade and the soil are as follows:

$$\sum_{i=1}^{n} X_i = F_P - F_R + f_2 \cos\alpha + F_2 \sin\alpha + f_1 = 0 \tag{4}$$

$$\sum_{i=1}^{n} Y_i = F_2 \cos\alpha - F_1 = 0 \tag{5}$$

$$f_i = \mu F_i \tag{6}$$

where F_p is the penetration resistance of the rotary blade when cutting the soil (N); F_R is the sum of the resistance applied to the rotary blade (N); f_i is the sliding friction applied to the inner and outer sides of the rotary blade (N); F_i is the positive pressure applied to the blade (N); α is the angle of the cutting edge (°); and μ is the coefficient of the sliding friction.

The effect of the friction force f_2 in the vertical direction is neglected since it does not act on the surface of the blade. Substituting Equation (6) into Equation (5) gives f_1

$$f_1 = f_2 \cos\alpha \tag{7}$$

Substitute Equation (7) into Equation (4) to find F_R:

$$F_R = F_P + F_1(2\mu + \tan\alpha) \tag{8}$$

As can be seen from Equation (8), the cutting resistance F_R is related to the normal pressure on the blade surface, the angle of the cutting edge, and the coefficient of the sliding friction. The greater the normal pressure on the blade edge and the coefficient of the sliding friction, the greater the cutting resistance of the rotary blade. If the angle of the cutting edge is too small, it will affect the strength of the cutting edge, leading to damages, such as

chipping and curling, during use, shortening its service life. Conversely, if the angle of the cutting edge is too large, it will increase the cutting resistance of the blade and reduce its cutting quality.

2.3.3. Mechanism of Rotary Blade Wear Loss

The tillage environment of rotary blades generally includes gravel, pesticide residues, crops, and other complex factors. After a long period of friction and contact stress between the blade and the gravel soil, the surface of the rotary blade is scratched or the material is shed, and the blade could even break and lead to failure, as shown in Figure 5 [29]. Most of the abrasive particles come from the gravel particles present in the soil itself and may also include the materials that fall off the surface of the rotary blade during wear. The wear on the surface of rotary blades is often not only due to one mechanism, but several mechanisms that exist simultaneously, and when conditions change, the different wear mechanisms will always change.

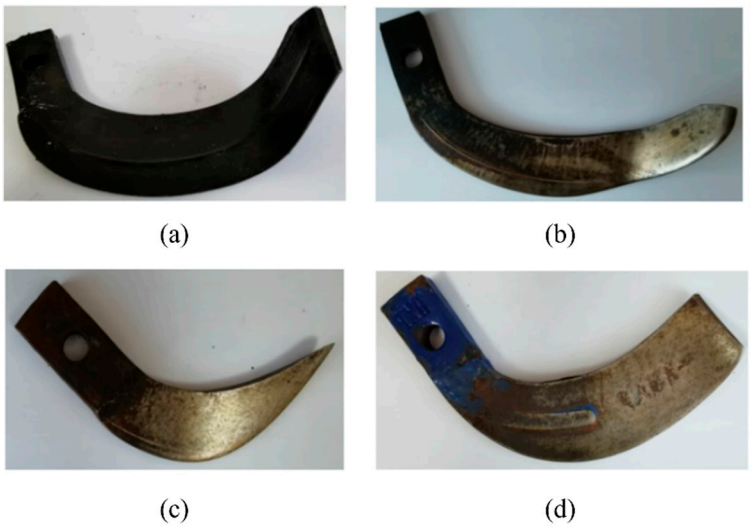

Figure 5. Wear condition of rotary blade [29]. (**a**) Unused state; (**b**) medium wear state; (**c**) heavy wear state; and (**d**) blade head fracture state.

Numerous scholars have carried out extensive research on the wear mechanism of rotary blades. HOORMAZDI et al. [30] predicted abrasive wear based on a combination of numerical and experimental methods, and observed the wear caused by the particle mixture on the soil-engaging components, greatly reducing the simulation time. In order to extend the service life of the plowshare, Yao et al. [31] studied the wear profile, three-dimensional wear pattern, and microscopic wear pattern of a 65 Mn plowshare in different plowing zones.

2.4. Rotary Blade–Soil Coupling Simulation Model

2.4.1. Soil Contact Modeling

Currently, existing studies mainly use the Hertz–Mindlin bonding model, the Hertz–Mindlin (no slip) model, and the Hysteretic Spring model to establish soil particle contact models. However, the Hertz–Mindlin (no slip) model cannot characterize the cohesive forces between soils effectively. Although the Hertz–Mindlin with bonding and Hysteretic Spring models can simulate the cohesion between soil particles, the actual operational process is quite complex, which increases the difficulty of the computation. The soil is a non-homogeneous, multiphase material with complex physical properties. The soil particles studied in this paper are sandy loam (moisture content: 16 ± 1%). Sandy loam contains a significant amount of sand particles and also a small number of clay particles;

the soil particles will be bonded and compressed to each other in the wet state, making the interactions between the particles more complex. Therefore, the Hertz–Mindlin with JKR is used to establish a soil particle contact model, which can consider the movement of cohesive particles, as well as simulate the forces between adherent particles. In addition, it is necessary to investigate the wear degree of the rotary blade surface caused by sandy loam; the Archard Wear model can be used to simulate the contact action form between soil particles and the rotary blade, enabling the prediction of wear on the blade surface.

The calculation of rotary blade–soil wear constant for the EDEM simulation is based on the Archard Wear theory. The sliding wear volume of the blade surface is as follows:

$$W_{\mathrm{v}} = \alpha_{\mathrm{s}} \cdot F_{\mathrm{n}} \cdot l \tag{9}$$

where l is the relative sliding distance between particles (mm).

According to the indentation characteristics of the sphere on the ductile plane in Figure 6, when the soil particles are in mutual contact with the blade surface, the sliding wear volume W_{v} can be expressed as follows:

$$W_{\mathrm{v}} = \phi \cdot A_0 \cdot l \tag{10}$$

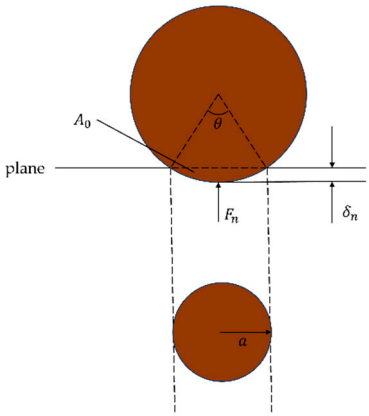

Figure 6. Schematic diagram of the indentation of spherical particles on the specimen surface.

The collation of Equations (9) and (10) can be obtained as follows:

$$\alpha_{\mathrm{s}} = \frac{A_0 \cdot \phi}{F_{\mathrm{n}}} \tag{11}$$

where α_{s} is the wear constant; A_0 is the cross-sectional area of the indentation (mm^2); ϕ is the ratio of the actual to the theoretical material removal, the size of which is taken to be 0.84 [32]; and F_{n} is the contact force on soil particles (N).

A_0, a and θ can be computed from Figure 6:

$$A_0 = \frac{\theta \cdot R_{\mathrm{p}}^2}{2} - a\left(R_{\mathrm{p}} - \delta_{\mathrm{n}}\right) \tag{12}$$

$$a = \sqrt{R_{\mathrm{p}}\delta_{\mathrm{n}}} \tag{13}$$

$$sin\frac{\theta}{2} = \frac{a}{R_{\mathrm{p}}} \tag{14}$$

where a is the radius of the contact area between particles (mm); δ_{n} is the directional overlap (mm); θ is the center angle of the arc (°); and R_{p} is the radius of the particles (mm).

Combining Equations (13) and (14) gives the following:

$$\theta = 2\arcsin\left(\frac{\delta_n}{R_p}\right)^{\frac{1}{2}} \tag{15}$$

Arrange Equations (12)–(14) to obtain A_0:

$$A_0 = \left[\arcsin\left(\frac{\delta_n}{R_p}\right)^{\frac{1}{2}} - \left(\frac{\delta_n}{R_p}\right)^{\frac{1}{2}} + \left(\frac{\delta_n}{R_p}\right)^{\frac{3}{2}}\right] R_p^2 \tag{16}$$

The reaction force F_n on the particle is as follows:

$$F_n = \frac{4}{3}E^* R_p^{\frac{1}{2}} \delta_n^{\frac{1}{2}} = \frac{4}{3}E^*\left(\frac{\delta_n}{R_p}\right)^{\frac{3}{2}} R_p^2 \tag{17}$$

where E^* is the equivalent modulus of elasticity.

This can be obtained by substituting Equations (16) and (17) into Equation (11) and collapsing it:

$$\alpha_s = \frac{3\phi\left[\arcsin\left(\frac{\delta_n}{R_p}\right)^{\frac{1}{2}} - \left(\frac{\delta_n}{R_p}\right)^{\frac{1}{2}} + \left(\frac{\delta_n}{R_p}\right)^{\frac{3}{2}}\right]}{4E^*\left(\frac{\delta_n}{R_p}\right)^{\frac{3}{2}}} \tag{18}$$

In order to determine the value of $\frac{\delta_n}{\delta_p}$ in the above equation, it is necessary to know the relationship between particle hardness and yield stress:

$$H_e \approx 3\sigma_c \tag{19}$$

where H_e is the particle hardness (Pa); σ_c is the yield stress (Pa), and the yield stress of the particle is approximately equal to the maximum compressive stress:

$$\sigma_c \approx P_m \tag{20}$$

The maximum compressive stress P_m for spherical particles is as follows:

$$P_m = \frac{2}{\pi}E^*\left(\frac{\delta_n}{R_p}\right)^{\frac{1}{2}} \tag{21}$$

Combining Equations (19)–(21), the following can be obtained:

$$\frac{\delta_n}{R_p} = \left(\frac{\pi H_e}{6E^*}\right) \tag{22}$$

The hardness of the quartz sand is 4.2×10^8 Pa, and by substituting it into Equations (22) and (18), the wear constant α_s is finally found to be 1.4×10^{-7}.

2.4.2. Soil Trough Model

A small soil trough model of 50 mm × 50 mm × 200 mm is built based on EDEM to simulate the movement behavior of soil particles. The boundary conditions are set so that particles can be generated in the way they are naturally deposited, and the soil parameters are imported into the EDEM soil database. Subsequently, a particle factory model of 300 mm × 300 mm × 1200 mm is created using Block Factory to simulate the characteristics of soil particles over a larger area.

For soil particle parameters, Wang et al. [33] found that soil particles have nine basic shapes in natural environments, but most of the soils show granular and agglomerated shapes in most areas, and 80% of the particle sizes are between 0.25 and 5 mm [34]. For ease of calculation, the particle model is simplified into single-sphere, double-sphere, and triple-sphere configurations, the sphere multiplicity is randomly distributed between 0.9 and 1.1 times [35], the radius of soil particles can be selected as 2.5 mm, and, to save simulation time, the radius of the simulated particles is enlarged once to 5 mm. The stone model is obtained by filling the contours of the stones with single spherical particles, the radius distribution of the stones is randomly distributed between 0.3 and 0.9 times, and the final model of the soil trench is shown in Figure 7.

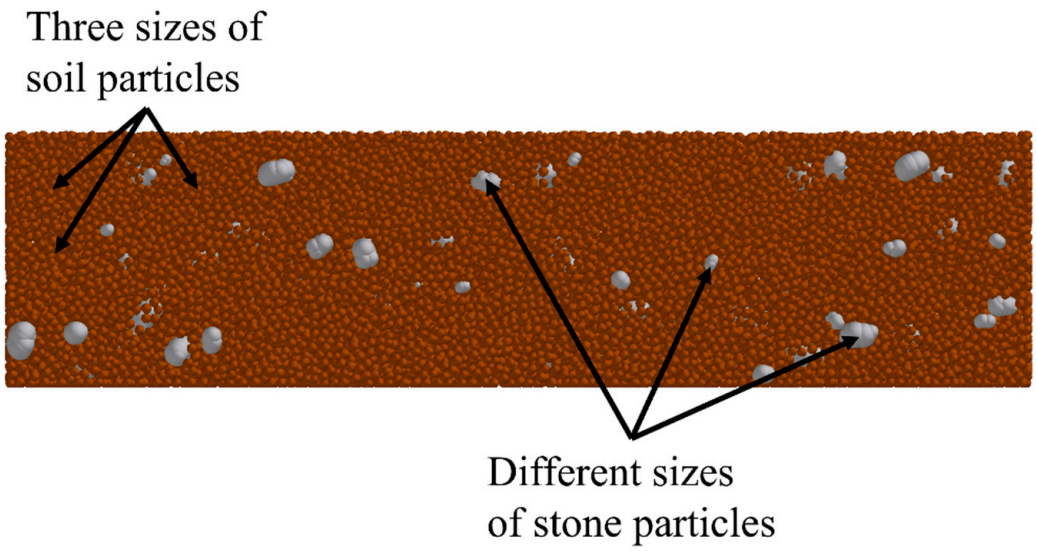

Figure 7. Cross-section of the soil trough model.

The material properties of the soil model and the contact parameters between the materials are crucial to ensuring the accuracy of the simulation. These parameters ensure that the soil particles can realistically exhibit deposition, collision, and interaction behaviors within the simulation environment. Soil properties vary across different regions, and the accuracy of soil models is significantly influenced by factors such as soil density and surface energy. Therefore, the soil density is measured using the cutting ring method, while the soil surface energy is obtained by measuring the soil's shear stress through direct shear tests and then combining it with simulation experiments using a trial-and-error method. Other material parameters are obtained from the relevant literature, and a detailed list of these parameters can be found in Table 1 [36].

Table 1. Material parameters.

Material Property/Contact Parameters	Soil	65Mn Rotary Blade	Particle—Particle	Particle—Rotary Blade
Poisson's ratio	0.35	0.28		
Material density (kg·m^{-3})	1600	7850		
Shear modulus (Mpa)	56	78,600		
Surface energy (J/m^2)	5.75	/		
Coefficient of static friction			0.30	0.50
Coefficient of kinetic friction			0.14	0.05
Coefficient of restitution			0.25	0.50

2.4.3. EDEM-RecurDyn Coupling Model

It is important to consider that using the EDEM discrete element simulation alone can only simulate the interaction mechanism between the soil and blade, which cannot effectively reflect the kinetic analysis of the blade. Therefore, in order to make the rotary blade exhibit the characteristics of that in a field operation, this study employs a bidirectional coupling simulation of EDEM and RecurDyn to fully validate the motion between particles and structures. In the pre-processing stage, the rotary blade–soil trough model is imported into RecurDyn, where the model is semi-automatically meshed using RecurDyn's tetrahedral elements, and the corresponding constraint conditions are added. The rotational speed and forward speed of the cutter shaft are set, the model is imported into EDEM after saving it as a .wall file, and the parameters of the soil particles and materials are added at the same time. The X-direction is set as the forward direction of the rotary blade, the horizontal speed is 0.5 m/s, the rotational speed of the blade roller along the Z-axis is 150 r/min, and the Y-direction is set as the maximum tilling depth of the rotary blade, which is 100 mm. The RecurDyn simulation step size is 100, the total simulation time is 1s, and the data saving interval is 0.01s. The EDEM and RecurDyn exchanged soil particle information and dynamic signals in a bidirectional manner. The coupling simulation process and principle are shown in Figure 8.

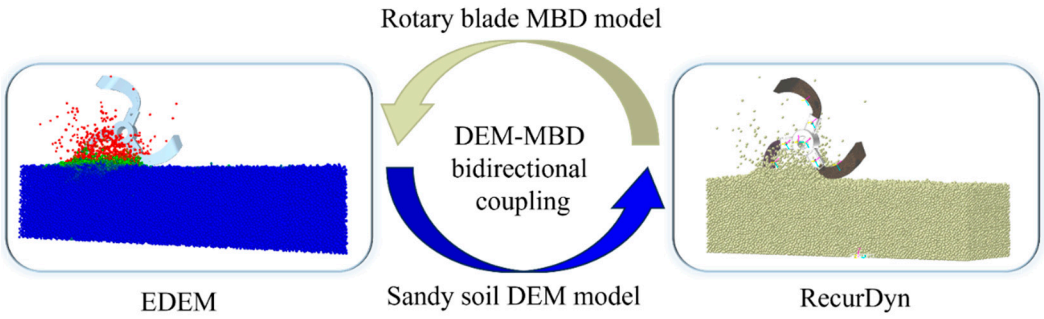

Figure 8. EDEM-RecurDyn coupling schematic diagram.

Secondly, due to the complexity of the constraints that need to be added, it is more difficult to create constraints between parts using EDEM, making it challenging to precisely represent the motion effects of the parts. Therefore, this article mainly utilizes RecurDyn to create the necessary motion constraints, as shown in Table 2. A fixed joint is added between the soil trough and the ground to prevent the soil trough from moving. A translate joint is added between the lid and the ground to prevent particles from splashing. A fixed joint is added between the blade roller and the rotary blade to prevent the rotary blade from falling off. Meanwhile, in order to save simulation time and simplify the transmission system, the power input is directly applied to the blade roller, so the G-motion is added between the blade roller and the ground. This constraint allows for both translate and revolute joints to be added simultaneously. Compared to adding translate and revolute joints in EDEM, the G-motion constraint is more convenient to operate.

Table 2. Constraint condition.

Matrix	Constrained Body	Type of Constraint
Ground	Soil trough	Fixed joint
Ground	Lid	Translate joint
Blade roller	Rotary blade	Fixed joint
Ground	Blade roller	G-motion: Revolute + translate joint

The rotational properties of the rotary blade include rotational speed, direction, and angle. The rotational speed of the rotary blade is controlled by the transmission system, and the blade's speed is adjusted by changing the output speed of the rotary tiller. The rotational direction of the rotary blade can be either forward or in reverse. In this article, the rotary blade consistently rotates clockwise (forward direction), in line with the forward motion of the rotary tiller. The rotational angle of the blade changes dynamically during the tilling process. Using the horizontal line as a reference, when the rotational angle is 30°, the rotary blade enters the soil; when the rotational angle reaches 150°, the blade exits the soil. Therefore, the tilling angle of the rotary blade is between 30° and 150°.

The rotational properties have a significant impact on the cutting behavior of the rotary blade. First, a high rotational speed will lead to greater friction and pressure on the blade, accelerating wear, while a low rotational speed will affect the tiller's working efficiency. Second, when rotating forward, the rotary tiller blade can deeply till the soil layer, loosening the soil and helping to retain moisture and nutrients, improving the soil's water content. The combination of tilling and soil fragmentation can enhance the efficiency of soil breaking, improving tilling quality. Finally, if the angle at which the blade enters the soil is too small, it will decrease the tilling quality. Conversely, if the angle is too large, it leads to excessive soil turnover, which not only increases energy consumption but also damages the soil structure.

2.5. Simulation Analysis of the Original Rotary Blade

2.5.1. Resistance Analysis of the Rotary Blade

Figure 9 shows a three-axis working resistance diagram for the rotary blade, which defines the forward direction of the rotary blade (positive direction of the X-axis) as the positive horizontal resistance F_1, the vertical downward direction along the soil surface (negative direction of Y-axis) as the positive vertical resistance F_2, and the vertical blade axis inward (negative direction of Z-axis) as the positive lateral resistance F_3.

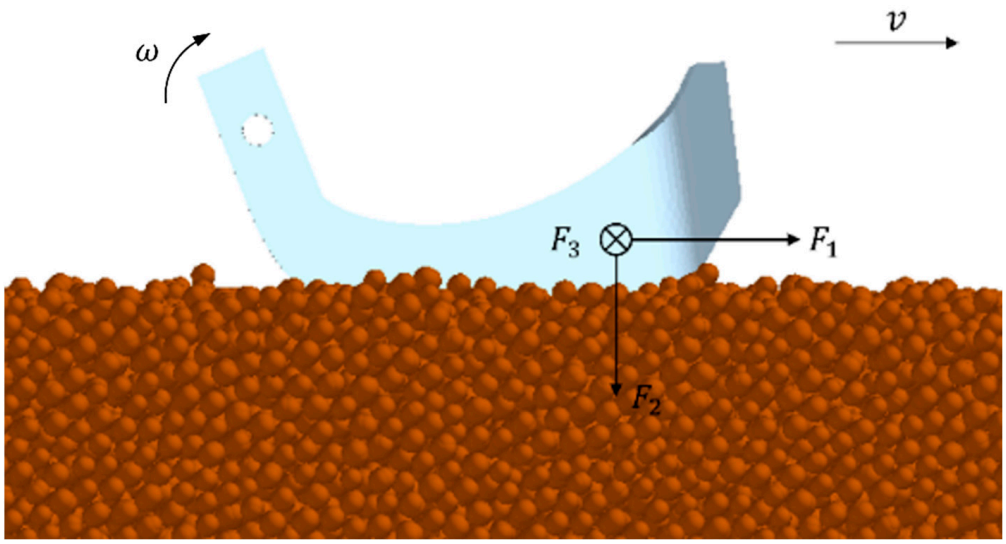

Figure 9. Three-axis working resistance diagram for rotary blade. F_i is the three-axis working resistance of the rotary blade (N); ω is the angular velocity of the rotary blade (rad·s^{-1}); and v is the forward speed of the blade roller.

When the rotary blade is tilling at a forward speed of 0.5 m/s, a rotational speed of 150 r/min, and a tilling depth of 100 mm, the change in the three-axis working resistance of the blade is shown in Figure 10. The horizontal resistance F_1 is always positive, indicating that the pressure of the soil particles on the blade surface from the inner side of the rotary

blade is greater than the extrusion borne by the outer side of the blade, mainly because of the fast rotational speed of the blade shaft, which results in the backward decomposition of the rotary blade in the process of cutting the soil to achieve a much greater speed than its forward speed, so the direction of the horizontal resistance F_1 is positive and increases with the increase in the angle of cutting the soil until a maximum value of 191.8 N occurs at 53°, and then gradually decreases to 0. The vertical resistance F_2, on the other hand, has both negative and positive values successively. In the process of the rotary blade cutting down the soil to the maximum tilling depth, it is generally subjected to upward resistance, and the resistance gradually increases to −230 N before the maximum tilling depth and then gradually decreases to 0. When the blade passes the maximum tilling depth, it is subjected to vertical downward resistance again, with the same trend of increasing to a maximum value of 64.9 N and then decreasing slowly. The lateral resistance F_3 is always negative because the rotary blade mulches the soil backward, and the soil on the inside of the blade has a tendency to squeeze outward against the bending zone, so the direction of the lateral resistance is perpendicular to the knife facing outwards.

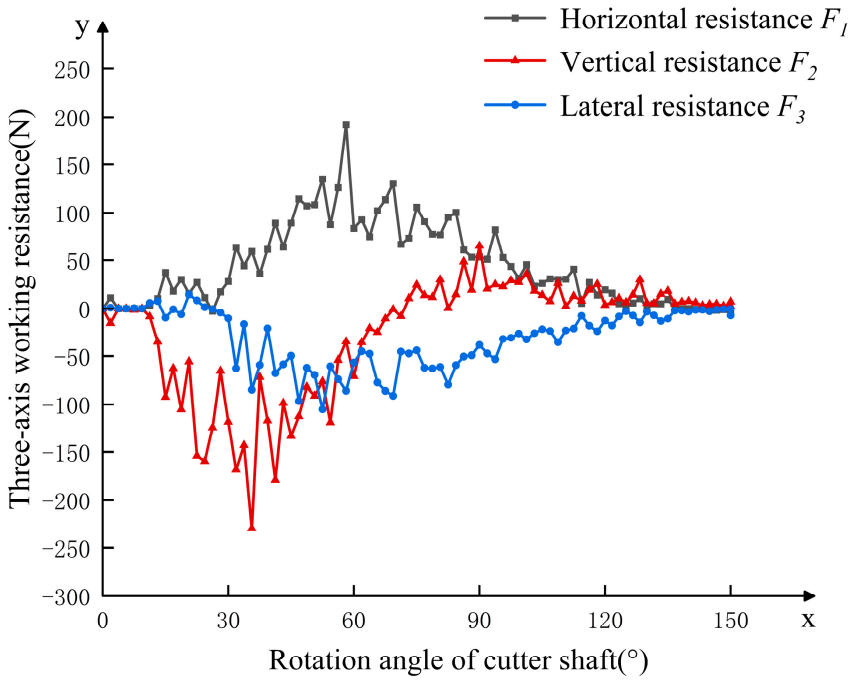

Figure 10. The variation trend of the three-axis working resistance with the rotation angle of the blade shaft.

As shown in Figure 11, which shows the rotary blade–soil dynamic flow diagram, combined with a resistance analysis, the soil cutting process of the rotary blade is consistent with the change law of tillage resistance. The side cutting edge of the blade is in contact with the soil, the resistance begins to increase, and then the sidelong edge cuts into the soil, performing double-edged work at the same time, and the resistance gradually increases to the maximum value. Then, the side cutting edge turns out of the soil, the resistance shows a downward trend, but the side cutting edge of the next blade cuts into the soil subsequently, and the resistance quickly rises again, keeping the two rotary blades working at the same time so as to repeat the movement.

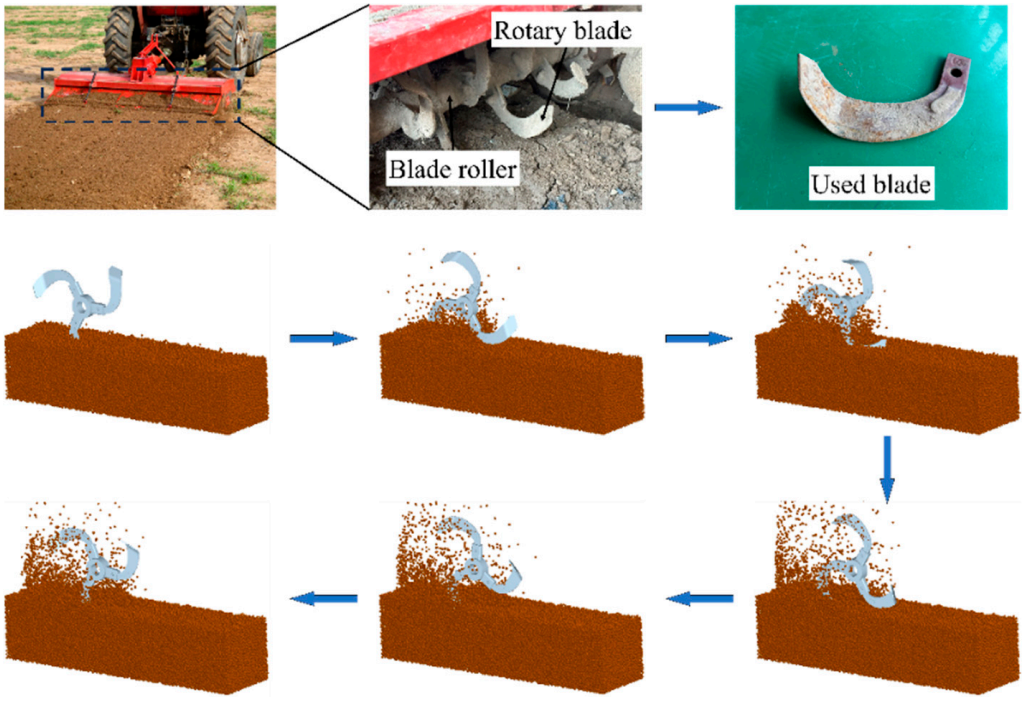

Figure 11. Dynamics mechanism on soil–rotary blade interaction.

2.5.2. Wear Analysis of Rotary Blade

The wear conditions of the rotary blade in different areas are obtained from the wear test, as shown in Figure 12. The results indicate that the wear of the rotary blade occurs mainly on the sidelong edge, the side cutting edge, and the bending zone edge. Overall, the blade body shows no significant wear, indicating that its contact and friction with the soil are relatively minimal. The wear amount in different areas of the rotary blade is shown in Figure 13. The sidelong edge is the most worn among the three regions, this is mainly because the tip of the blade is subjected to high stress, enduring significant compressive and frictional forces from the soil. Next, the wear on the bending zone edge and side cutting edge is similar, both of which are less than the wear on the tip of the blade. The main reason is that the contact area between the side cutting edge and the bending zone edge of the rotary blade with the soil is relatively small, resulting in lower friction and cutting resistance. As a result, the wear and tear are relatively light.

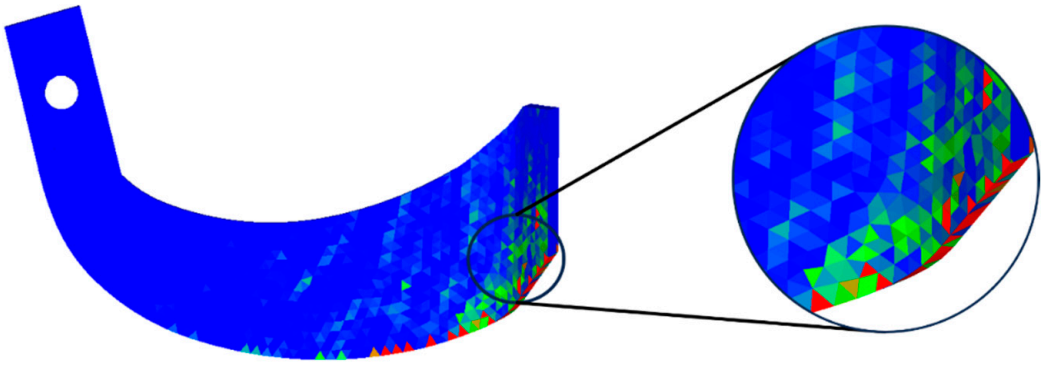

Figure 12. Wear micrograph of rotary blade.

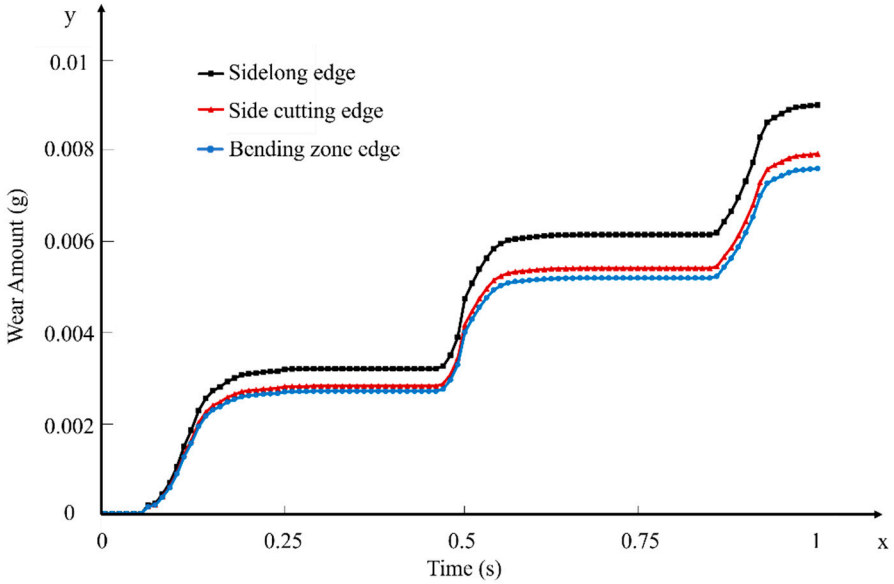

Figure 13. The wear amount in different areas of the rotary blade.

2.6. Simulation Model Validation

In order to verify the accuracy of the DEM-MBD coupling simulation model, a soil trough with a length of 100 m, a width of 4 m and a depth of 1 m, as shown in Figure 14a, is selected for the wear test. A sensor, as shown in Figure 14b, is used to measure the torque value of the drive shaft, and the torque and rotational speed values of the drive shaft are transmitted to the computer in real time. The accuracy of the simulation model is assessed by comparing the change rule of the torque, which is also a comprehensive index reflecting the size of the tillage resistance of the rotary blade. Before the start of the test, the left and right rotary blades are installed on the blade roller, and then the rotational speed of the blade shaft is set at 150 r/min and the forward speed of the trolley is set at 0.5 m/s, and the torque of the rotary blades is measured when the tillage depth is 80 mm, 100 mm, 120 mm, 140 mm, and 160 mm. The comparison in Figure 15a shows that the variation trend of the torque curve of the simulation model is basically consistent with that of the soil trough test, indicating that the simulation effect can better reflect the variation trend of the tillage resistance of the rotary blade and verifying the feasibility of the coupling of discrete elements and multi-body dynamics. Figure 15b shows that the scatter plots of the five data sets are all within the 95% confidence interval of the difference between the experiment and the simulation, indicating that the data have good consistency. However, there are still some errors, primarily due to the frequent use of the soil trough in field experiments, resulting in the presence of influences such as straw or weeds.

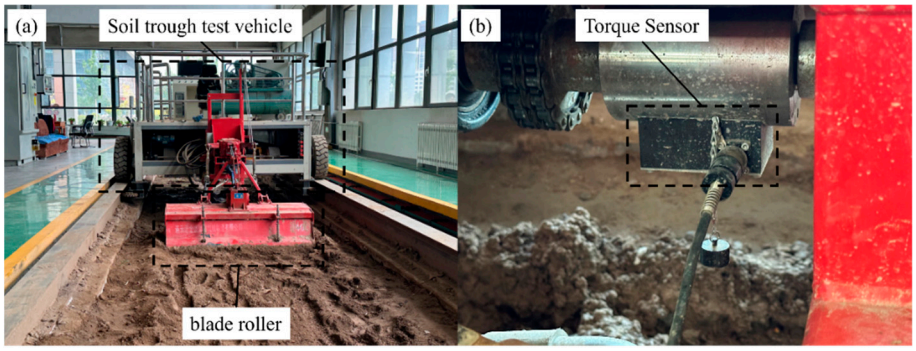

Figure 14. Soil trough test vehicle.

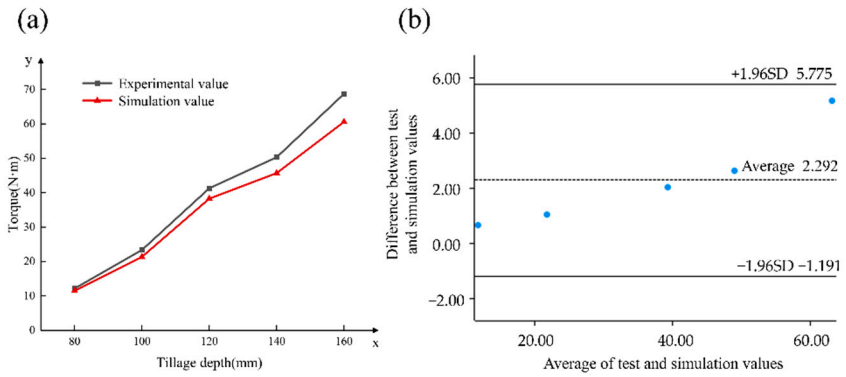

Figure 15. Validation of the simulation model: (**a**) comparison of torque between simulation and test at different tillage depths; and (**b**) Bland–Altman diagram.

2.7. Optimized Design of Rotary Blades

In order to investigate the influence of various factors on the tillage resistance of rotary blades and seek the optimal structural parameters of rotary blades, this paper adopts the multiple regression orthogonal rotation method to optimize the structural parameters of rotary blades in a multifactorial way. The height of the tangent edge end face h (A), bending radius r (B), and bending angle β (C) are taken as test factors, and the wear amount and tillage resistance are taken as evaluation indexes. The height of the tangent edge end face h is taken to be between 48 and 56 mm, the bending radius r is taken to be between 20 and 30 mm, and the bending angle β is taken to be between 116 and 124°. A three-factor and three-level central composite design is formulated as shown in Table 3, and the experimental scheme and results are shown in Table 4.

Table 3. Experimental factors and codes.

Experimental Factors	Level		
	−1	**0**	**1**
A—Height of Tangent Edge End Face /mm	48	52	56
B—Bending Radius /mm	20	25	30
C—Bending Angle /°	116	120	124

Table 4. Experiment design and results.

No.	A/(mm)	B/(mm)	C/(°)	Wear Amount /($\times 10^{-2}$ g)	Tillage Resistance /N
1	52	30	124	2.42	246.2
2	52	20	116	1.94	209.5
3	52	25	120	2.36	219.1
4	48	30	120	2.50	212.7
5	52	25	120	2.31	219.5
6	52	20	124	2.44	241.1
7	48	20	120	2.41	217.8
8	52	25	120	2.35	225.5
9	56	20	120	2.47	225.3
10	52	25	120	2.34	220.3
11	52	25	120	2.38	221.9
12	48	25	124	2.46	239.7
13	48	25	116	1.90	207.6
14	56	25	116	1.98	205.6
15	56	30	120	2.55	212.6
16	52	30	116	1.95	202.0
17	56	25	124	2.42	243.9

3. Results and Discussion

3.1. Analytical Results of the Central Composite Design

3.1.1. Analysis of Variance for Parameter Optimization

An analysis of variance was performed by the Design-Expert software to verify its significance. The results, as shown in Table 5, showed that the *p*-values (significance values) in the regression models for wear and tillage resistance were less than 0.0001, showing that the models were highly significant and indicating that the models were valid. The lack-of-fit of the wear and tillage resistance were 0.211 and 0.2857, respectively, which were both greater than 0.05, indicating that the effect of unknown factors on the model was not significant and the experimental error was small. The coefficients of determination R^2 of the wear and tillage resistance were 0.99 and 0.9788, respectively, and the correction coefficients R^2 were 0.9772 and 0.9516, indicating that the regression model had a good fit, and the correlation between the experimental values and the predicted values was high, which verified the feasibility of using this model to determine the structure optimization parameters. The effects of C, A^2, B^2 and C^2 were highly significant for the wear amount of the tool Y_1, and the effects of C and C^2 on tillage resistance Y_2 were extremely significant. The remaining coefficients of the primary and quadratic terms had low significant effects. By eliminating non-significant factors, the regression equations between each factor and wear amount Y_1 and tillage resistance Y_2 were established base on the data obtained from Table 4, respectively, as follows:

$$Y_1 = 0.0235 + 0.0002A + 0.0002B + 0.0025C - 0.0003AC - 0.0001BC + 0.0007A^2 + 0.0007B^2 - 0.0023C^2 \quad (23)$$

$$Y_2 = 221.26 + 1.2A - 2.53B + 18.28C - 1.9AB + 1.55AC + 3.15BC - 2.33A^2 - 1.83B^2 + 5.27C^2 \quad (24)$$

3.1.2. Analysis of Response Surfaces and Contour Caps for Different Evaluation Indexes

The three-dimensional response surface diagram and contour diagram of the interaction between different factors and response values are shown in Figures 16–19, respectively. The response surfaces visualize the trend of the factors' influence on the target, while the contour lines indicate the interaction between the factors and the target values. As shown in Figures 16–19, the trends of the response surfaces and contour lines under the influence of factors A, C and B, C were generally consistent, and the trends of the response surfaces and contour lines under the influence of factors A and B were quite different from the other two trends. Comparing the response surfaces of two different factor combinations, it could be seen that A, B, and C all had a certain influence on the response value; but from observing Figures 16a and 18a, it could be seen that the change in the response values was not obvious when the influence of factor C was not taken into account, which indicated that A and B had a lower influence on the response values, and at the same time, when combined with Figures 16b,c and 18b,c, it was not difficult to see that the response surfaces were steep, which indicated that factor C had the most significant effect on the response value. In addition, according to Figures 17b,c and 19b,c, it could be seen that when A and B were combined with C, respectively, the response value was slightly more affected by B than A, which indicated that the degree of B's influence on the response value was more significant, but both of them were much smaller than C.

Table 5. Variance analysis of multivariate quadratic polynomial regression equation.

Evaluation Index	Variation Source	S_s	D_f	M_s	F	p	Significance
Wear Amount	Model	0.0001	9	8.204×10^{-6}	77.03	<0.0001	**
	A	2.812×10^{-7}	1	2.812×10^{-7}	2.64	0.1482	
	B	3.200×10^{-7}	1	3.200×10^{-7}	3.00	0.1266	
	C	0.0000	1	0.0000	455.50	<0.0001	**
	AB	2.500×10^{-9}	1	2.500×10^{-9}	0.0235	0.8826	
	AC	3.600×10^{-7}	1	3.600×10^{-7}	3.38	0.1086	
	BC	2.250×10^{-8}	1	2.250×10^{-8}	0.2113	0.6597	
	A^2	1.976×10^{-6}	1	1.976×10^{-6}	18.55	0.0035	**
	B^2	1.834×10^{-6}	1	1.834×10^{-6}	17.22	0.0043	**
	C^2	0.0000	1	0.0000	202.83	<0.0001	**
	Residual error	7.455×10^{-7}	7	1.065×10^{-7}			
	Lack-of-fit	4.775×10^{-7}	3	1.592×10^{-7}	2.38	0.2110	
	Pure error	2.680×10^{-7}	4	6.700×10^{-8}			
	Cor Total	0.0001	16				
Tillage Resistance	Model	2944.56	9	327.17	35.93	<0.0001	**
	A	11.52	1	11.52	1.27	0.2978	
	B	51.01	1	51.01	5.60	0.0498	
	C	2671.80	1	2671.80	293.41	<0.0001	**
	AB	14.44	1	14.44	1.59	0.2483	
	AC	9.61	1	9.61	1.06	0.3385	
	BC	39.69	1	39.69	4.36	0.0752	
	A^2	22.86	1	22.86	2.51	0.1571	
	B^2	14.10	1	14.10	1.55	0.2534	
	C^2	116.94	1	116.94	12.84	0.0089	**
	Residual error	63.74	7	9.11			
	Lack-of-fit	36.67	3	12.22	1.81	0.2857	
	Pure error	27.07	4	6.77			
	Cor Total	3008.30	16				

S_s is the sum of squares. D_f is the freedom. M_s is the mean square. F is the F-value. p is the p-value ** is highly significant.

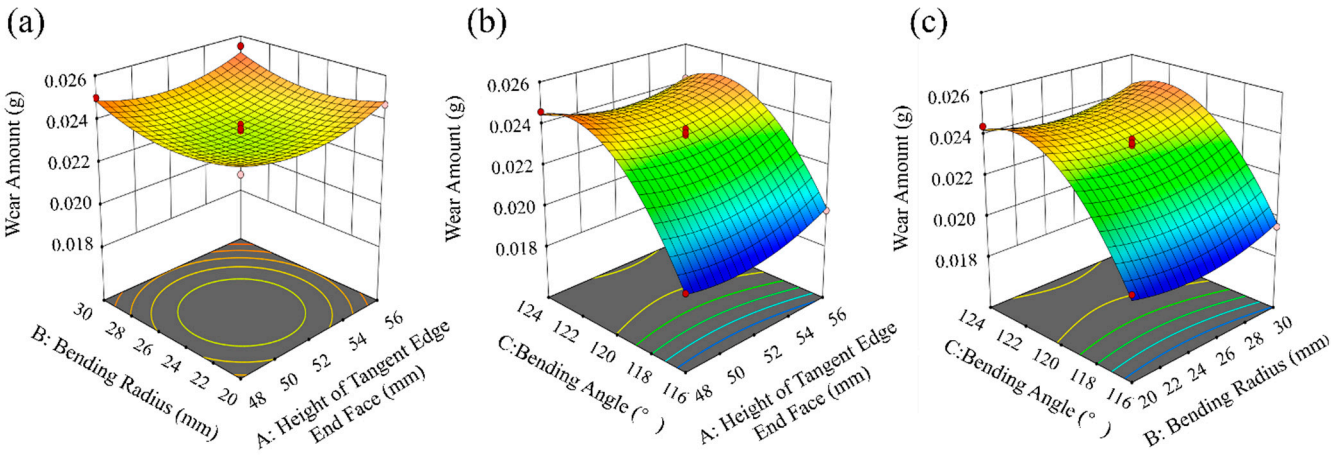

Figure 16. Response surfaces diagram of wear amount. (**a**) The effect of A and B on the wear amount when C is 120°; (**b**) the effect of A and C on the wear amount when B is 25 mm; and (**c**) the effect of B and C on the wear amount when A is 52 mm; the wear amount fluctuates between 0.019 and 0.0225 g.

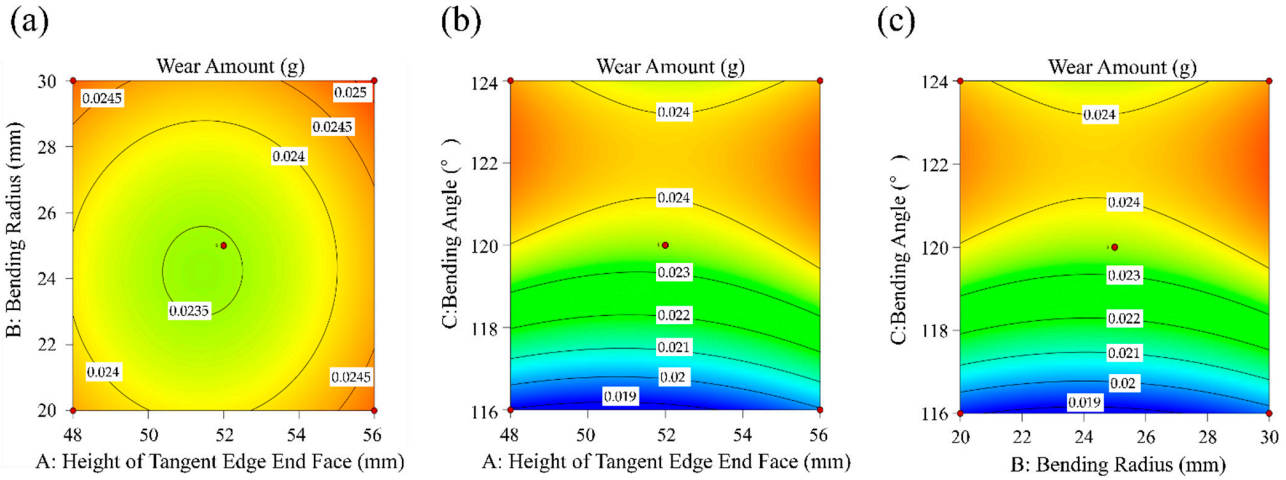

Figure 17. Contour map of wear amount. (**a**) The effect of A and B on the wear amount when C is 120°; (**b**) the effect of A and C on the wear amount when B is 25 mm; and (**c**) the effect of B and C on the wear amount when A is 52 mm; the wear amount fluctuates between 0.019 and 0.0225 g.

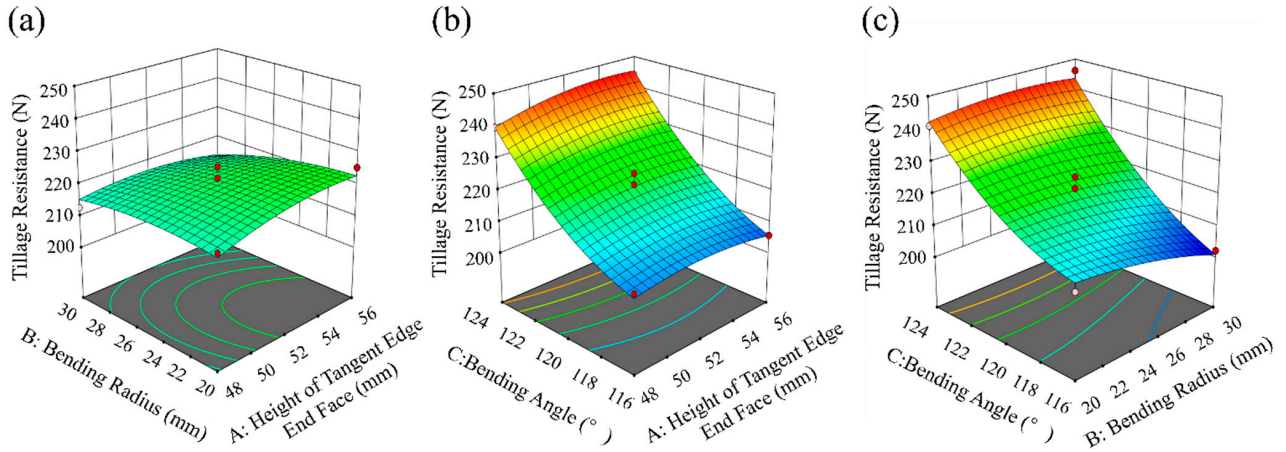

Figure 18. Response surfaces diagram of tillage resistance. (**a**) Effect of A and B on tillage resistance when C is 120°; (**b**) effect of A and C on tillage resistance when B is 25 mm; (**c**) effect of B and C on tillage resistance when A is 52 mm; tillage resistance fluctuates between 202 and 246.2 N.

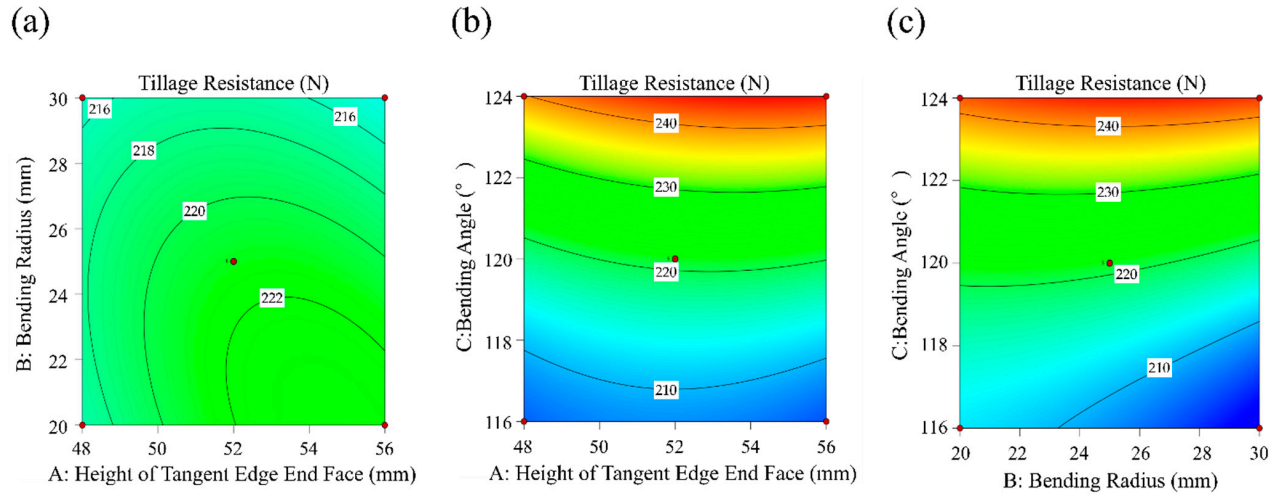

Figure 19. Contour map of tillage Resistance. (**a**) Effect of A and B on tillage resistance when C is 120°; (**b**) effect of A and C on tillage resistance when B is 25 mm; and (**c**) effect of B and C on tillage resistance when A is 52 mm; tillage resistance fluctuates between 202 and 246.2 N.

3.2. Regression Curves and Marginal Effect of Factors

Before the structural optimization, it was necessary to analyze the influence of each factor on the blade. After the linear coding of the parameters, it was found that there was no linear correlation between the principal coefficient and the quadratic coefficient in the regression equation, but the quadratic coefficient or the interaction coefficient between the regression coefficients were linearly correlated [37]. Therefore, a marginal effect analysis could be used to determine the effect of each factor on rotary blade wear and tillage resistance. The single-factor model regression equation was established as follows:

$$\begin{cases} Y_{11} = 0.0235 + 0.0002A + 0.0007A^2 \\ Y_{12} = 0.0235 + 0.0002B + 0.0007B^2 \\ Y_{13} = 0.0235 + 0.0025C - 0.0023C^2 \end{cases} \tag{25}$$

$$\begin{cases} Y_{21} = 221.26 + 1.2A - 2.33A^2 \\ Y_{22} = 221.26 - 2.53B - 1.83B^2 \\ Y_{23} = 221.26 + 18.28C + 5.27C^2 \end{cases} \tag{26}$$

The model of each factor in the regression equation was derived as the marginal equation of an extreme value:

$$\begin{cases} Y'_{11} = 0.0002 + 0.0014A \\ Y'_{12} = 0.0002 + 0.0014B \\ Y'_{13} = 0.0025 - 0.0046C \end{cases} \tag{27}$$

$$\begin{cases} Y'_{21} = 1.2 - 4.66A \\ Y'_{22} = -2.53 - 3.66B \\ Y'_{23} = 18.28 + 10.54C \end{cases} \tag{28}$$

The single-factor regression equations are shown in Figure 20a,c, with factors A and B obtaining extreme values near x = 0 and factor C obtaining maximum or minimum values at x = 0.5 and x = −1. The marginal equation curves are shown in Figure 20b,d, where Y_1 and Y_2 were affected by factors A and B in the same trend, subjected to the opposite trend of factor C to A and B. Both Y_1 and Y_2 were most affected by factor C, and Y_1 was affected by factors A and B in the same way and Y_2 is slightly less affected by factor B than factor A. The main reason why Y_1 and Y_2 were most affected by the bending angle was that the bending angle of the rotary blade directly influenced its soil cutting depth and the soil turnover effect. Yu [38] found that when the bending angle was too large, the rotary blade had difficulty achieving the soil throwing effect during tilling, which significantly increased the tillage resistance. Conversely, when the bending angle was too small, the tilling depth of the blade was affected, and the surface stress on the blade intensified, reducing its service life. Meanwhile, there were some differences in the degree of influence of the three factors on the evaluation indexes, so it was necessary to optimize the parameters to reduce the resistance and wear amount in actual production.

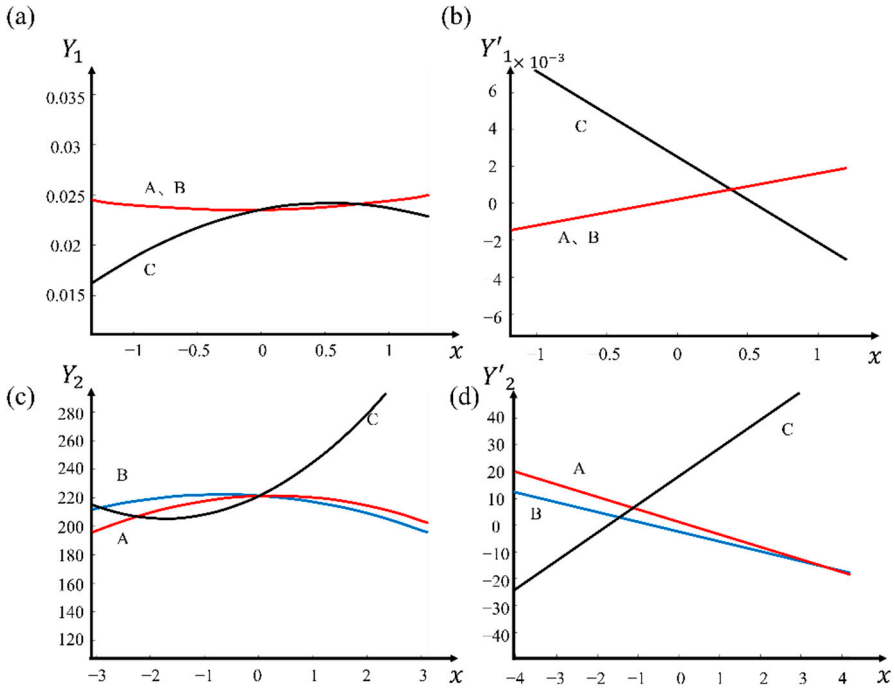

Figure 20. Regression curves of single-factor model and the marginal effect plot of factors. (**a**) Regression curve for Y_1; (**b**) marginal effect plot for Y_1; (**c**) regression curve for Y_2; (**d**) marginal effect plot for Y_2.

3.3. Optimal Parameter Combination

The structural parameters of the rotary blade were optimized using Design-Expert, with the minimum wear amount and minimum tillage resistance as the final optimization objectives, respectively, and the optimization equations were established as shown in Equation (29). The final results showed that the minimum values of wear amount and tillage resistance were 0.019 g and 204.24 N, respectively, when the height of the tangent edge end face A was 50.57 mm, the bending radius B was 28.13 mm, and the bending angle C was 116°. For the convenience of the experiment, the final values were rounded such that the height of the tangent edge end face was 51 mm, the bending radius was 28 mm, and the bending angle was 116°.

$$\begin{cases} minY_1(A,B,C) \\ minY_2(A,B,C) \\ 48 \le A \le 56 \\ 20 \le B \le 30 \\ 116 \le C \le 124 \end{cases} \tag{29}$$

3.4. Comparative Tests of the Rotary Blade

3.4.1. Comparison of the Tillage Resistance

In order to verify the effect of reducing the resistance and wear of the optimized rotary blade, it was compared with the unoptimized rotary blade. The results showed that the tillage resistance of the optimized and unoptimized rotary blades had similar trends, but the average tillage resistance of the optimized rotary blade was reduced by 12% compared with that of the unoptimized rotary blade, as shown in Figure 21. Further calculations showed that the wear of the optimized rotary blade was reduced by 22.4%, as shown in Figure 22.

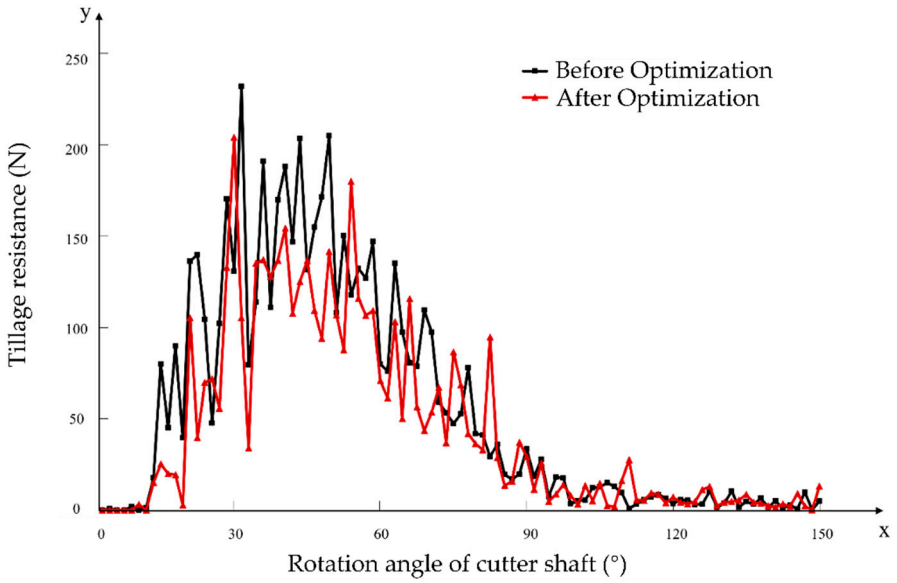

Figure 21. Comparison of tillage resistance before and after optimization of rotary blade.

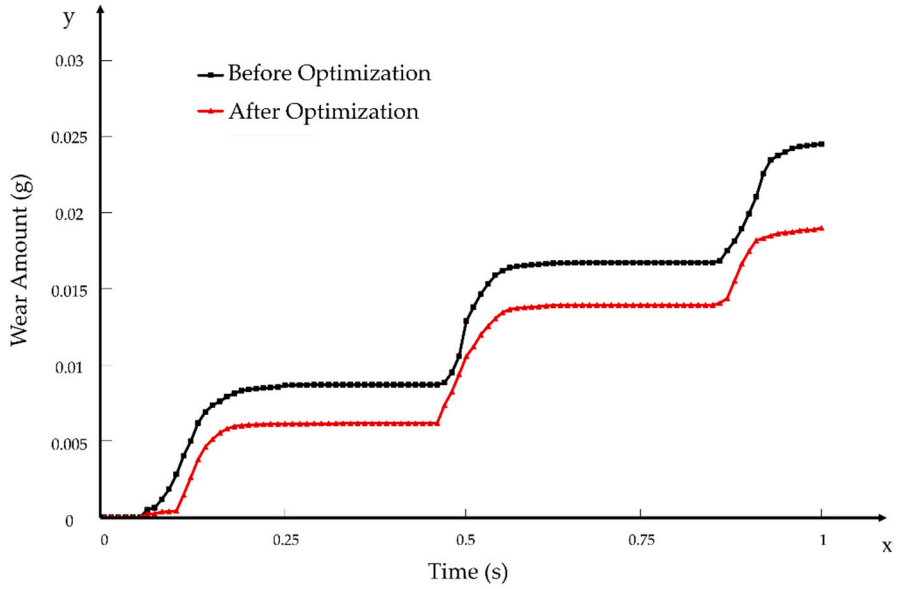

Figure 22. Comparison of the wear amount of the optimized and unoptimized rotary blade.

Yu et al. [38] designed a wedge drag reduction rotary blade, and the experiments showed that the optimized rotary blade reduced the tillage resistance by 8.81%. Hao et al. [28] designed a new type of rotary blade, which reduced the tillage resistance by 10.65%. The results indicated that the optimized rotary blade in this study showed an improvement compared to previous research. The optimized rotary blade achieved the expected goal of reducing resistance and wear and provided a new idea for future research on optimizing rotary blades.

3.4.2. Comparison of Soil Disturbance Situation

Compared with the curve graph, the soil disturbance situation can aid in visualizing the tillage performance of the rotary blade. To analyze the difference between the optimized and unoptimized rotary blade parameters, a comparative analysis of the soil disturbance caused by the rotary blade was conducted using soil motion cloud maps. Four time nodes in the simulation process of the optimized and unoptimized rotary blade were selected for analysis, as shown in Figure 23: at 0.075 s, the side cutting edge comes into contact with the

soil, and the soil surface began to sag slightly due to downward pressure. When the tangent edge cut into the soil at 0.1 s, the inner soil was cut by the blade and moved backward under the influence of the cutting action and the extrusion pressure of the blade. At 0.15 s, the rotary blade completely entered the soil, the inner soil flowed further backward, and the surface soil was pressed up by the inner soil and gradually formed small soil ridges. At 0.21 s, when the rotary blade withdrew from the soil, the upward movement trend of the surface soil gradually disappeared due to the reduction in the force and it returned to the soil pit under the action of gravity.

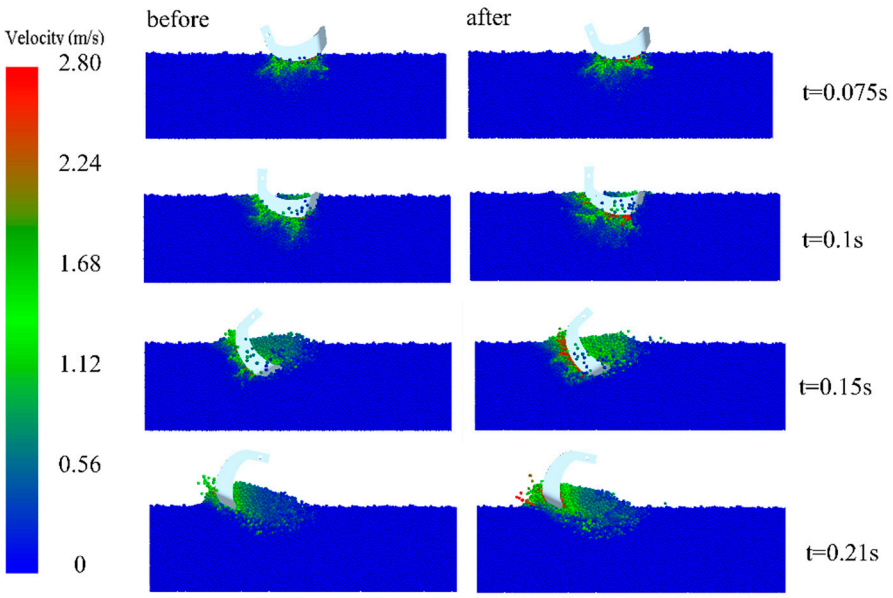

Figure 23. Cloud map of soil movement at various stages.

In order to further investigate the soil disturbance of the optimized and unoptimized rotary blades, the velocity of soil particles at different time points was selected for a comparative analysis. As shown in Figure 23, the red particles of the optimized rotary blade have increased compared to the unoptimized rotary blade, indicating that the particle velocity gradually increases. At the same time, during the process of soil cutting by the rotary blade, both the soil on the inside of the blade and the soil at the blade edge were subjected to squeezing force, and the particle movement speed was the highest in the bending edge and at the blade edge of the rotary blade. Comparing the motion process of the optimized and unoptimized rotary blades, one could find that the optimized rotary blade not only increased the speed of the particles but also expanded the range of particles with higher speeds, indicating that the longitudinal disturbance range of the optimized rotary blade was increased, which could make the particles move more easily.

3.4.3. Comparison of Cross-Sections for Soil Disturbance

A representative cross-section was selected, and the soil disturbance contour comparison of the optimized and unoptimized rotary blades were obtained by the tracing method, as shown in Figure 24. Under the same tillage environment, the soil disturbance profile of the optimized rotary blade was obviously wider than that of the unoptimized rotary blade, increasing the disturbance range of the rotary blade and the ridge height of the surface soil. Additionally, the optimized rotary blade had significantly increased the soil disturbance range in both the horizontal and vertical directions, further validating that the optimized rotary blade had not only met the design requirements for reduced resistance and wear but also effectively improved tillage quality and operational efficiency.

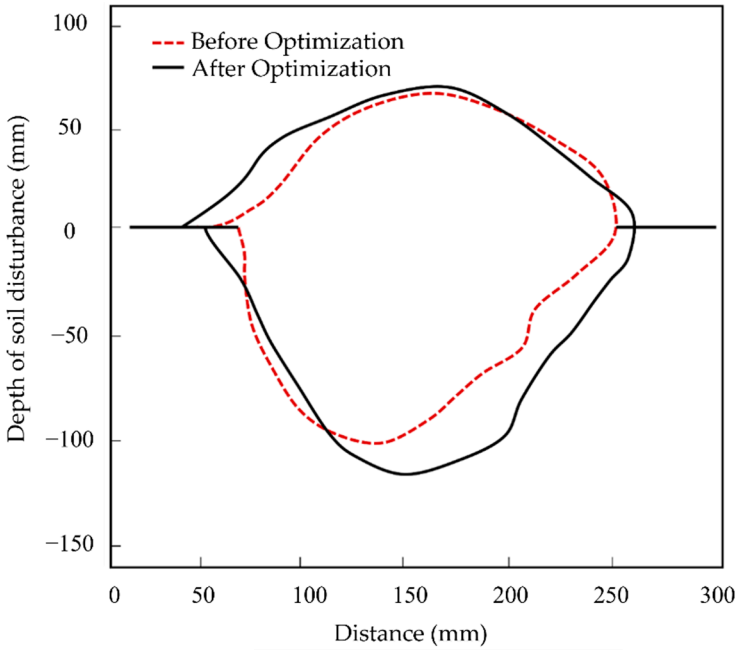

Figure 24. Comparison of soil disturbance cross-sections of the optimized and unoptimized rotary blade.

3.4.4. Field Test of the Optimized and Unoptimized Rotary Blade

Figure 25 shows the comparison results of the shaft torque of the optimized and unoptimized rotary blades in the field test process, and the change law of the shaft torque could objectively reflect the tillage resistance of the rotary blades. It could be seen from the figure that the shaft torque of the optimized rotary blade was reduced compared with that of the unoptimized rotary blade. Therefore, according to the results of field experiments, the tillage resistance of the optimized rotary blade was lower.

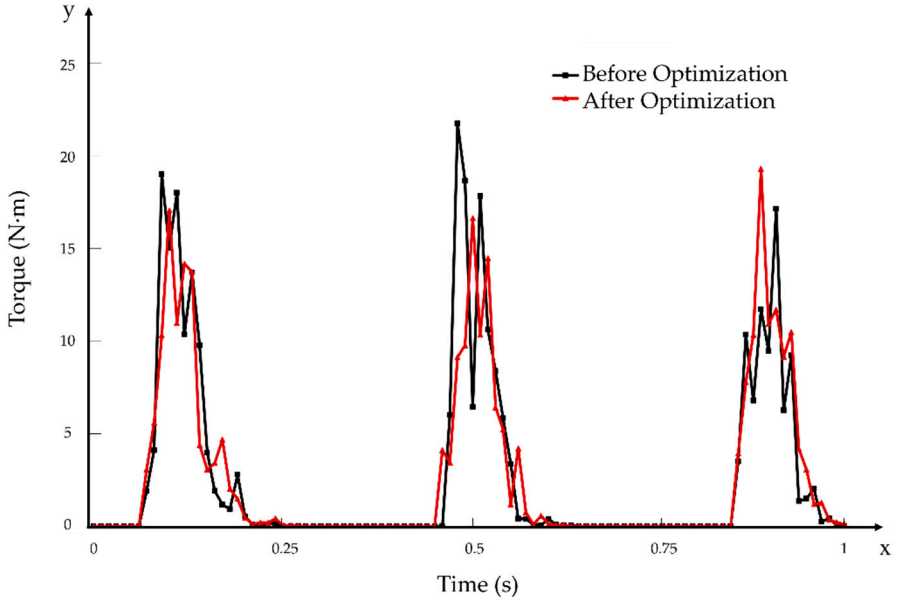

Figure 25. Torque comparison diagram of the optimized and unoptimized blade shaft.

In summary, the optimized rotary blade improved the width of soil disturbance. It not only enhanced the looseness of the soil, increasing its porosity, aeration, and water retention, which helped improve the supply of oxygen and water in the soil, but also improved the tillage efficiency and quality of the rotary tiller. At the same time, the tillage

resistance of the optimized rotary blade and the torque on the blade shaft were reduced. These two aspects could indirectly lead to a decrease in the power consumption of the rotary tiller, thereby achieving the effects of energy saving and emission reduction.

4. Conclusions

(1) The torque of a rotary blade was measured when the forward speed was 0.5 m/s, the rotation speed of the blade shaft was 150 r/min, and the tillage depth was 80 mm, 100 mm, 120 mm, 140 mm, and 160 mm by using an EDEM-RecurDyn coupling simulation and field experiment, respectively. The analysis of the experimental data found that the simulation value was slightly lower than the experimental value, which was probably due to the influence of factors such as gravel and weeds in the soil of the soil trough test.

(2) The simulation results of analyzing the three-axis working resistance of the rotary blade showed that the horizontal resistance always pointed to the forward direction of the rotary blade, the lateral resistance pointed vertically to the outward direction along the inner side of the blade surface, and the vertical resistance direction was the vertical soil plane upwards and then downward. The change trend of the three-axis working resistance was that it increased to the maximum value first and then gradually approached 0, in which the peaks of lateral resistance and horizontal resistance appeared near the maximum tilling depth, and the maximum value of vertical resistance was always preceded by the first two. Using the three-axis working resistance analysis to analyze the simulation results of the rotary blade could reflect the macroscopic stress of the blade more directly.

(3) The height of the tangent edge end face, bending radius, and bending angle were selected as test factors, the wear and tillage resistance of the rotary blade were evaluated as evaluation indexes, and a three-factor and three-level central composite design was carried out to optimize the parameters of the rotary blade with an EDEM-RecurDyn coupling simulation. The optimal combination of structural parameters was obtained when the height of the tangent edge end face was 51 mm, the bending radius was 28 mm, and the bending angle was 116°. A comparative analysis of the optimized and unoptimized rotary blades revealed that the wear and tillage resistance decreased by 22.4% and 12%, respectively.

Author Contributions: Conceptualization, Z.M.; methodology, Z.M., Y.Z., K.Z., J.W. and J.Y.; software, Z.M., J.W., J.Y., X.Z., S.C. and Z.Y.; validation, Z.M., Y.Z., K.Z., J.W. and X.Z.; formal analysis, Z.M., Y.Z., K.Z., J.W., X.Z. and B.L.; investigation, Z.M.; resources, Y.Z.; data curation, Z.M., Y.Z. and J.W.; writing—original draft preparation, Z.M., Y.Z.; writing—review and editing, Z.M., Y.Z. and K.Z.; visualization, Z.M., K.Z., J.W., J.Y., S.C. and Z.Y.; supervision, Y.Z., K.Z. and J.Y.; project administration, Y.Z. and K.Z.; funding acquisition, Y.Z. All authors have read and agreed to the published version of the manuscript.

Funding: This research was funded by the Gansu Key Research and Development Program-Industrial Project (24YFGA044; 23YFGA0070), the Lanzhou Municipal Science and Technology Program (2023-QN-185), the Higher Education Industrial Support Plan Project of Gansu Province (2021CYZC-29), and the Gansu Agricultural University Youth Mentor Support Fund (GAU-QDFC-2024-07).

Institutional Review Board Statement: Not applicable.

Data Availability Statement: The data presented in this study are available upon request from the corresponding author. The data are not publicly available due to possible further research.

Conflicts of Interest: The authors declare no conflicts of interest.

Nomenclature

The symbols, Greek Letters, abbreviations, and terms used in this study are shown below.

Nomenclature	
Symbols	
A_0	Cross-sectional area of the indentation (mm^2)
A	Height of tangent edge end face (mm)
a	Radius of the contact area between particles (mm)
B	Bending radius (mm)
C	Bending angle (°)
D_f	Freedom
E^*	Equivalent modulus of elasticity
F	F-value
F_i	Three-axis working resistance of rotary blade (N)
f_i	Sliding friction (N)
F_n	Contact force on soil particles (N)
F_P	Penetration resistance of rotary blade (N)
F_R	Sum of resistance (N)
H	Tilling depth of rotary blade (mm)
H_e	Particle hardness (Pa)
l	Relative sliding distance between particles (mm)
M_s	Mean square
N_i	Positive pressure (N)
n	Rotational speed of blade shaft ($r \cdot min^{-1}$)
p	p-value
P_m	Maximum compressive stress (Pa)
R_p	Radius of particles (mm)
R	Rotational radius of rotary blade (mm)
S	Cutting spacing of soil (mm)
S_s	Sum of squares
t	Time (s)
V_m	Forward speed of rotary blade ($m \cdot s^{-1}$)
W_V	Soil particles in mutual contact with the blade surface
Y_1	Wear amount (g)
Y_2	Tillage resistance (N)
Z	Number of blades
Greek Letters	
θ	Center angle of the arc (°)
σ_c	Yield stress (Pa)
ω	Angular velocity of rotary blade ($rad \cdot s^{-1}$)
λ	Rotary tillage speed ratio
α	Angle of the cutting edge (°)
μ	Coefficient of sliding friction
α_s	Wear constant
$\varnothing$	Ratio of the actual to the theoretical material removal
δ_n	Directional overlap (mm)
Abbreviations	
DEM	Discrete element method
MBD	Multibody dynamics
CCD	Central composite design
CCF	Central composite face-centered design
RSM	Surface response method
SPH	Smoothed particle hydrodynamics

Terms	
Tillage resistance	The force that acts on the surface of the rotary blade and impedes its movement
Wear mount	Changes in quality of rotary blade before and after plowing
Soil disturbance	The process of displacement, deformation, or destruction between soil particles
Torque	Torque on the rotary blade shaft

References

1. Adajar, J.B.; Alfaro, M.; Chen, Y.; Zeng, Z.W. Calibration of discrete element parameters of crop residues and their interfaces with soil. *Comput. Electron. Agric.* **2021**, *188*, 11. [CrossRef]
2. Matin, M.A.; Fielke, J.M.; Desbiolles, J.M.A. Torque and energy characteristics for strip-tillage cultivation when cutting furrows using three designs of rotary blade. *Biosyst. Eng.* **2015**, *129*, 329–340. [CrossRef]
3. Zhang, G.S.; Zhang, Z.Q.; Xiao, M.H.; Bartos, P.; Bohata, A. Soil-cutting simulation and parameter optimization of rotary blade's three-axis resistances by response surface method. *Comput. Electron. Agric.* **2019**, *164*, 10. [CrossRef]
4. Zhu, H.; Wang, D.W.; He, X.N.; Shang, S.Q.; Zhao, Z.; Tan, Y.; Wang, H.Q. Simulation analysis and test validation of reverse rotary tiller operation power consumption. *J. Agric. Mech. Res.* **2024**, *46*, 15–21+82.
5. Li, S.T.; Chen, X.B.; Chen, W.; Zhu, S.P.; Li, Y.W.; Yang, L.; Xie, S.Y.; Yang, M.J. Soil-cutting simulation and parameter optimization of handheld tiller's rotary blade by Smoothed Particle Hydrodynamics modelling and Taguchi method. *J. Clean. Prod.* **2018**, *179*, 55–62. [CrossRef]
6. Sun, J.; Jiang, H.; Zheng, X.; Nong, H.L.; Zeng, B.S.; Yang, W. Simulation of ultra deep rotary tillage tool based on soil disturbance. *J. Agric. Mech. Res.* **2024**, *46*, 66–71.
7. Wang, X.Z.; Fang, W.Q.; Han, D.L.; Chen, X.G. Review of the research on soil disturbance by tools. *Appl. Sci.* **2022**, *13*, 338. [CrossRef]
8. Zhang, X.N.; You, Y.; Wang, D.C.; Wang, Z.Y.; Liao, Y.Y.; Li, S.B. Soil failure characteristics and loosening effectivity of compacted grassland by subsoilers with different plough points. *Biosyst. Eng.* **2024**, *237*, 170–181. [CrossRef]
9. Yang, Y.W.; Tong, J.; Ma, Y.H.; Jiang, X.H.; Li, J.L. Design and experiment of biomimetic rotary tillage blade based on multiple claws characteristics of mole rats. *Trans. Chin. Soc. Agric. Eng. (Trans. CSAE)* **2019**, *35*, 37–45.
10. Zhang, Z.H.; Chen, Z.Y.; Lai, Q.H.; Sun, W.Q.; Xie, G.F.; Tong, J. Design and experiments of the Bouligand structure inspired bionic wear resistant soil-engaging component for the agricultural machinery. *Trans. Chin. Soc. Agric. Eng. (Trans. CSAE)* **2023**, *39*, 28–37.
11. Kim, Y.S.; Siddique, M.A.; Kim, W.S.; Kim, Y.J.; Lee, S.D.; Lee, D.K.; Hwang, S.J.; Nam, J.S.; Park, S.U.; Lim, R.G. DEM simulation for draft force prediction of moldboard plow according to the tillage depth in cohesive soil. *Comput. Electron. Agric.* **2021**, *189*, 18. [CrossRef]
12. Ucgul, M.; Saunders, C. Simulation of tillage forces and furrow profile during soil-mouldboard plough interaction using discrete element modelling. *Biosyst. Eng.* **2020**, *190*, 58–70. [CrossRef]
13. Ucgul, M.; Saunders, C.; Fielke, J.M. Comparison of the discrete element and finite element methods to model the interaction of soil and tool cutting edge. *Biosyst. Eng.* **2018**, *169*, 199–208. [CrossRef]
14. Zhang, L.B.; Cai, Z.X.; Wang, L.W.; Zhang, R.X.; Liu, H.F. Coupled Eulerian-Lagrangian finite element method for simulating soil-tool interaction. *Biosyst. Eng.* **2018**, *175*, 96–105. [CrossRef]
15. Wu, Z.Y.; Wang, X.S.; Liu, D.W.; Xie, F.P.; Ashwehmbom, L.G.; Zhang, Z.Z.; Tang, Q.J. Calibration of discrete element parameters and experimental verification for modelling subsurface soils. *Biosyst. Eng.* **2021**, *212*, 215–227. [CrossRef]
16. Chen, X.Y.; Chen, M.D.; Liu, M.M.; Li, Y.; Yang, D.Q.; Wu, H.H. Design and Experiment of Sweet Potato Ridging and Forming Machine. *Agriculture* **2023**, *13*, 1641. [CrossRef]
17. Song, P.; Lyu, J.Q. Effects of coupling simulation of self-excited vibratory subsoiler based on EDEM-RecurDyn. *J. Northeast. Univ.* **2023**, *54*, 87–94.
18. Yuan, J.; Yu, J.Q. Analysis on operational process of self-excited vibrating subsoiler based on DEM-MBD coupling algorithm. *Trans. Chin. Soc. Agric. Mach.* **2020**, *51*, 17–24.
19. Liu, Y.; Liu, Y.P.; Zhang, T. Load analysis of rotary cutter shaft for power tiller based on DEM and MBD theory. *J. Agric. Sci. Technol.* **2020**, *22*, 79–86.
20. Zhang, Z.H.; Zhao, L.L.; Lai, Q.H.; Tong, J. Operation mechanism analysis and experiments of shovel-type rolling soil-engaging components based on DEM-MBD coupling. *Trans. Chin. Soc. Agric. Eng. (Trans. CSAE)* **2022**, *38*, 10–20.
21. Dong, X.Q.; Su, C.; Zheng, H.N.; Han, R.Q.; Li, Y.L.; Wan, L.P.C.; Song, J.N.; Wang, J.C. Analysis of soil disturbance process by vibrating subsoiling based on DEM-MBD coupling algorithm. *Trans. Chin. Soc. Agric. Eng. (Trans. CSAE)* **2022**, *38*, 34–43.
22. Tekeste, M.Z.; Balvanz, L.R.; Hatfield, J.L.; Ghorbani, S. Discrete element modeling of cultivator sweep-to-soil interaction: Worn and hardened edges effects on soil-tool forces and soil flow. *J. Terramechanics* **2019**, *82*, 1–11. [CrossRef]

23. Cucinotta, F.; Scappaticci, L.; Sfravara, F.; Morelli, F.; Mariani, F.; Varani, M.; Mattetti, M. On the morphology of the abrasive wear on ploughshares by means of 3D scanning. *Biosyst. Eng.* **2019**, *179*, 117–125. [CrossRef]
24. Tekeste, M.Z.; Way, T.R.; Syed, Z.; Schafer, R.L. Modeling soil-bulldozer blade interaction using the discrete element method (DEM). *J. Terramechanics* **2020**, *88*, 41–52. [CrossRef]
25. Xiong, P.Y.; Yang, Z.; Sun, Z.Q.; Zhang, Q.Q.; Huang, Y.Q.; Zhang, Z.W. Simulation analysis and experiment for three-axis working resistances of rotary blade based on discrete element method. *Trans. Chin. Soc. Agric. Eng. (Trans. CSAE)* **2018**, *34*, 113–121.
26. Yang, Z.K.; Zhang, K.P.; Zhang, Y.; An, J. Discrete Element Method-Multibody Dynamics Coupling Simulation and Experiment of Rotary Tillage and Ridging Process for Chili Pepper Cultivation. *Agronomy* **2024**, *14*, 446. [CrossRef]
27. Makarov, S.A.; Danilin, A.V.; Levchenko, G.V.; Kalinichenko, E.B.; Ivaniva, L.M. Investigation of kinematic parameters of the rotary working body of a universal rotary cultivator. *IOP Conf. Ser. Earth Environ. Sci.* **2022**, *979*, 012058. [CrossRef]
28. Hao, J.J.; Yu, H.J.; Zhao, J.G.; Li, J.C.; Ma, Z.K.; Cai, J.J. Design and test of wedge drag reduction rotary blade. *Trans. Chin. Soc. Agric. Eng. (Trans. CSAE)* **2019**, *35*, 55–64.
29. Zhu, C.S. Study on Characteristics and Wear Resistance Modification of Wire Arc Additive Remanufacturing of Damaged Rotary Tillage Cutter. Doctoral Thesis, Jiangsu University, Zhenjiang, China, 2021.
30. Hoormazdi, G.; Küpferle, J.; Röttger, A.; Theisen, W.; Hackl, K.A. Concept for the Estimation of Soil-Tool Abrasive Wear Using ASTM-G65 Test Data. *Int. J. Civ. Eng.* **2019**, *17*, 103–111. [CrossRef]
31. Yao, Q.; Han, X.R.; Hu, Y.H.; Guo, Z.H.; Fan, P.W.; Zhang, Y.Q. Field wear tests of ploughshares in the southern Xinjiang region. *Eng. Fail. Anal.* **2024**, *163*, 12. [CrossRef]
32. Chen, G.M.; Schott, D.L.; Lodewijks, G. Sensitivity analysis of DEM prediction for sliding wear by single iron ore particle. *Eng. Comput.* **2017**, *34*, 2031–2053. [CrossRef]
33. Wang, G.M.; Guo, X.Y.; Zhao, C.J.; Wang, J.H. Soil visual simulation study based on particle system. *Trans. Chin. Soc. Agric. Eng. (Trans. CSAE)* **2008**, *24*, 152–158.
34. Shi, L.R.; Zhao, W.Y.; Sun, W. Parameter calibration of soil particles contact model of farmland soil in northwest arid region based on discrete element method. *Trans. Chin. Soc. Agric. Eng. (Trans. CSAE)* **2017**, *33*, 181–187.
35. Patidar, P.; Soni, P.; Jain, A.; Mahore, V. Modelling soil-rotor blade interaction of vertical axis rotary tiller using discrete element method (DEM). *J. Terramechanics* **2024**, *112*, 59–68. [CrossRef]
36. Fang, Y.Y.; Zhang, K.P.; Yang, Z.K. Simulation analysis and experiment of ploughing process in northwest arid region based on discrete element method. *Acta Agric. Univ. Jiangxiensis* **2024**, *46*, 1323–1340. [CrossRef]
37. Arbizu, I.P.; Pérez, C.J.L. Surface roughness prediction by factorial design of experiments in turning processes. *J. Mater. Process. Technol.* **2003**, *143*, 390–396. [CrossRef]
38. Yu, H.J. Optimal Design and Experiment of Wedge Drag Reduction Rotary Blade. Master's Thesis, Hebei Agricultural University, Baoding, China, 2019.